

Article

A Bimodal Hydrostatic Actuator for Robotic Legs with Compliant Fast Motion and High Lifting Force

Alex Lecavalier , Jeff Denis, Jean-Sébastien Plante and Alexandre Girard *

Mechanical Engineering Department, Université de Sherbrooke, Sherbrooke, QC J1K 2R1, Canada; alex.lecavalier@usherbrooke.ca (A.L.); jeff.denis@usherbrooke.ca (J.D.); jean-sebastien.plante@usherbrooke.ca (J.-S.P.)

* Correspondence: alexandre.girard2@usherbrooke.ca

Abstract: Robotic legs, such as for lower-limb exoskeletons and prostheses, have bimodal operation: (1) within a task, like for walking (high speed and low force for the swing phase and low speed and higher force when the leg bears the weight of the system); (2) between tasks, like between walking and sit–stand motions. Sizing a traditional single-ratio actuation system for such extremum operations leads to oversized heavy electric motor and poor energy efficiency at low speeds. This paper explores a bimodal actuation concept where a hydrostatic transmission is dynamically reconfigured using custom motorized ball valves to suit the requirements of a robotic leg with a smaller and more efficient actuation system. First, this paper presents an analysis of the mass and efficiency advantages of the bimodal solution over a baseline solution, for three operating points: high-speed, high-force, and braking modes. Second, an experimental demonstration with a custom-built actuation system and a robotic leg test bench is presented. Control challenges regarding dynamic transition between modes are discussed and a control scheme solution is proposed and tested. The results show the following findings: (1) The actuator prototype can meet the requirements of a leg bimodal operation in terms of force, speed, and compliance while using smaller motors than a baseline solution. (2) The proposed operating principle and control schemes allow for smooth and fast mode transitions. (3) Motorized ball valves exhibit a good trade-off between size, speed, and flow restriction. (4) Motorized ball valves are a promising way to dynamically reconfigure a hydrostatic transmission while allowing energy to be dissipated.

Keywords: robotic leg; wearable robot; legged locomotion; dual-speed actuator; hydrostatic transmission; two-speed transmission; gear shifting; force bandwidth; digital hydraulics; valve



Citation: Lecavalier, A.; Denis, J.; Plante, J.-S.; Girard, A. A Bimodal Hydrostatic Actuator for Robotic Legs with Compliant Fast Motion and High Lifting Force. *Actuators* **2023**, *12*, 452. <https://doi.org/10.3390/act12120452>

Academic Editor: Steve Davis

Received: 6 November 2023

Revised: 1 December 2023

Accepted: 4 December 2023

Published: 7 December 2023



Copyright: © 2023 by the authors. Licensee MDPI, Basel, Switzerland. This article is an open access article distributed under the terms and conditions of the Creative Commons Attribution (CC BY) license (<https://creativecommons.org/licenses/by/4.0/>).

1. Introduction

When designing legged robots and exoskeletons, the requirements can be very different for torque and speed depending on the task or within different phases of a task. This often limits the capabilities of a robotic device. For example, the Sarcos Guardian XO full-body exoskeleton can amplify human loading capacity but is limited for natural walking or running [1]. In contrast, Harvard’s cable-driven soft exosuit can assist for loaded walking [2] but has limited force assistance. For a legged robot, the feet need to move quickly through the air during a fast gait or to balance the system. The ideal robotic leg actuator must have good acceleration and maximum velocity capability for the swing phase (foot in the air). Lightly-gearred actuators and direct-drive electric motors (EM) have been used for creating highly dynamic legged robots [3,4]. On the other hand, during the stance phase (foot on the ground), the leg must apply large forces to bear the weight of the robot and its payload. Without large reduction ratios, EM actuators exhibit poor torque density and poor efficiency at low speeds [3,5].

Thus, they are not well suited for stance phase requirements, especially when the robot needs to lift and carry heavy payloads. Alternatively, using EM with large reduction ratios

to meet the stance phase requirements would limit the maximum velocity and increase the inertia and the friction [6], thus penalizing the performance of the swing phase. Hence, designing a robot that can be used for all these operating points is not trivial and leads designers to compromise between multiple characteristics, as illustrated in Figure 1, when using a fixed reduction ratio.



Figure 1. Trade-offs of geared motors with a fixed reduction ratio: direct drive and lightly geared motors on the left and highly geared motors on the right.

Dynamically changing the reduction ratio, like most car powertrains, would allow a designer to avoid this performance compromise. As shown in Figure 2, if a robot leg actuator can downshift to a large reduction ratio during the stance phase (operation point 1), and upshift to a small reduction ratio for the swing phase (operation point 2), then the electric motor does not need to be oversized to achieve both operation points and would stay within an effective operating range. In recent decades, actuators leveraging variable transmission have been sporadically explored by researchers in the field of robotics. For instance, Hirose relied on two parallel motors of different reduction ratio and an electromagnetic clutch to create a dual-mode transmission mechanism for an articulate prismatic leg [7]. Bell proposed a dual-motor design for which the geared motor is electrically disconnected for high-speed motions to prevent back-emf power dissipation, but the geared motor inertia stays coupled to the output which limits the possible reduction ratios [8]. Jeong et al. presented a single-motor two-speed transmission based on twisted string actuation (TSA) and a dog clutch that is light and compact, but with many limitations in the operating conditions [9]. Lee et al. proposed a compact dual reduction actuator with a latching mechanism for a knee joint exoskeleton adapted for the walking phase and sit-to-stand phase, but without dynamic switching capabilities [10]. For seamless transitions, Jang et al. developed a continuously variable transmission (CVT) based on TSA, two motors, and a differential gearbox, but is limited by the range of reduction ratios. Other serial dual-motor architectures were investigated, requiring a differential and a brake that can be used to conduct seamless transitions, and shown the mass and energy advantages over single-ratio actuators [5,11,12].

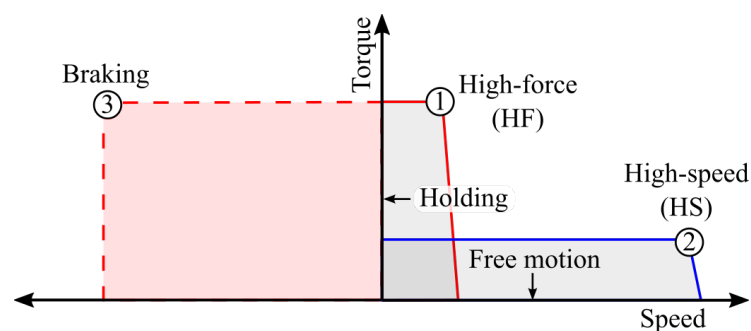


Figure 2. The three targeted operating points of the proposed multimodal design.

All in all, despite promising results, many challenges remain: (1) the trade-off between the complexity (and size) of the variable transmission and its ability to change the ratio in terms of range, speed, seamlessness, and operating conditions in which it is possible to change the reduction ratio [13]; (2) the need for a lightweight and energy efficient device for robots that carry their own payload. A lightweight device that allows a fast and seamless switch between a small and a large reduction ratio in any operating conditions would be a breakthrough for many applications, especially for robotic legs.

Previously proposed variable ratio designs for robotics were mostly based on mechanical components like gears and brakes. However, others have proposed variable ratio concepts leveraging a hydrostatic transmission as a way to delocalize the motor of the moving linkage rather than being on distal joints. The advantage of hydrostatic transmissions are mainly easy routing through complex kinematics [14], good force density, and increased backdrivability [15]. In this sense, Sugihara et al. proposed a reconfigurable hydrostatic circuit to allow a variable ratio using fast hydraulic switching with extra valves and cylinders, but much remains to be explored regarding this kind of hybrid hydrostatic approach [16].

This article presents a multimodal actuation based on simple valves dynamically reconfiguring a hydrostatic transmission. As illustrated in Figure 3, motorized ball valves are used to dynamically reconfigure the system between two operating modes tailored to the swing phase and stance phase. The concept is similar to the two-speed architecture explored by Verstraten [12] and Girard [5], but in the fluidic domain. The salient feature is that ball valves replace the high-force brake and the differential that were required in the mechanical domain, reducing the number of cumbersome components while increasing the flexibility in terms of conditions in which the system can downshift. This article is built on preliminary results presented in a conference paper [17], which analyzed opportunities to save mass and increase efficiency of actuation system using multimodal hydrostatic transmissions. Here, a thorough analysis of one of these opportunities is presented: using high-speed/high-force mode switching. The mass saving analysis is expanded with an exploration of the trade-off between size, speed, and flow for the valves. Furthermore, this article presents a working prototype, experimental results on a 2-DoF leg test bench as shown in Figure 4, control challenges and solutions, practical issues, and limitations, which were not discussed in the preliminary conference paper.

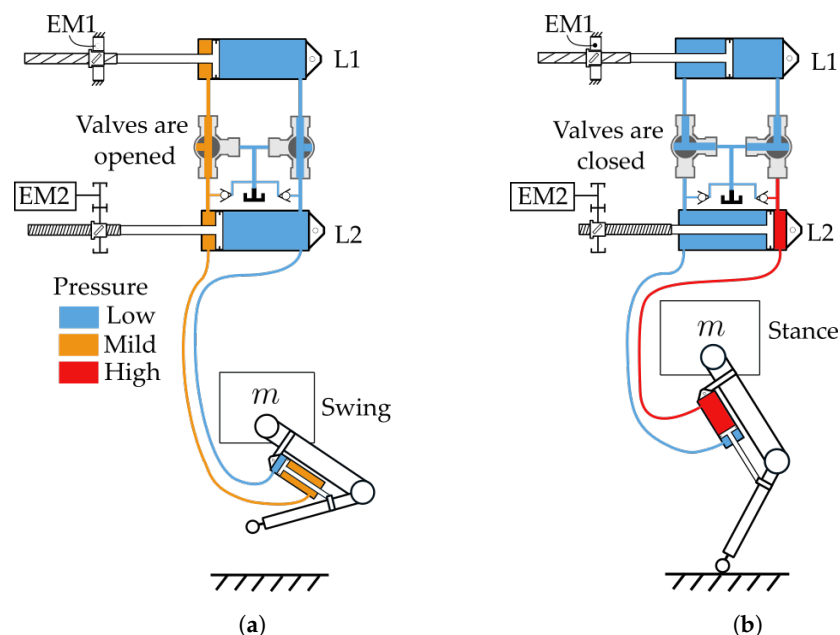


Figure 3. Bimodal actuation principle of the proposed hydrostatic architecture. (a) High-speed mode; (b) high-force mode.

The novel contributions of the present study are the following: (1) a mass delay–flow trade-off analysis for motorized ball valves plus a more detailed mass-efficiency analysis of the overall system; (2) an experimental assessment of the ability of the system to switch seamlessly under load; (3) first experiments giving an insight on the actuator capability to match the needs of robotic legs in terms of force, speed, and compliance.

The materials and methods are split through the manuscript sections for better readability. Section 2 explains the working principle and details the equations of motions of

the proposed bimodal hydrostatic system. Section 3 presents the mass and energy gain potential of the configuration to achieve extreme operating points for the case study of a robotic knee joint. Section 4 presents the built prototypes and test bench, the control scheme used for coordinating the motor and the valves, and the experimental results. Finally, the modeling approach for estimating the mass and efficiency of the components involved is presented in the Appendix A.

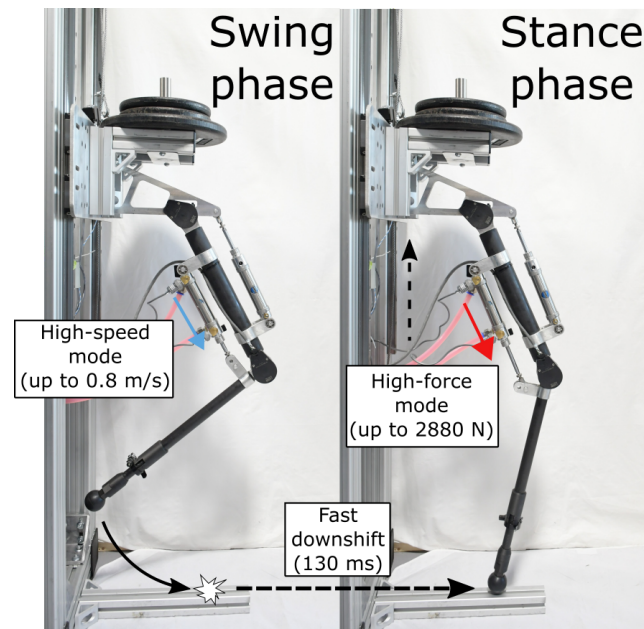


Figure 4. Bimodal demonstration on a robotic knee: swing phase (high-speed phase), stance phase (high-force phase).

2. Working Principle

The proposed two-speed architecture consists of a lightly geared electric motor (EM1) and a highly geared electric motor (EM2) which are coupled to high- and low-pitch ball screws, respectively, that actuate two hydraulic cylinders. Those two cylinders—called leader cylinder 1 (L1) and leader cylinder 2 (L2)—are connected to a follower cylinder (output) on the leg, through a flexible hydraulic line. This results in a kinematically redundant system: the displacement of both the leader cylinders adds up to create a displacement at the follower cylinder (neglecting compressibility of the fluid) but the pressure is shared in the circuit. Additionally, two hydraulic valves can close the path to the lightly geared L1. Hence, this architecture permits two main modes of operation: a high-speed mode (HS) for fast movement and backdrivability when the valves are opened (Figure 3a) and a high-force mode (HF) when the valves are closed (Figure 3b). When valves are open, both L1 and L2 can contribute to the output motion. This results in high-speed capability and a low reflected inertia at the output, but with force limited by EM1. When valves are closed, only L2 contributes to the output since L1 is connected to a reservoir and can move freely. This results in high-force low-speed capabilities, as the configuration leads to a direct coupling of the highly geared piston to the follower piston. Furthermore, it is possible to generate large forces at high-speed using partial opening of the valves to restrict the flow in order to brake the system. Therefore, it is possible to reach operating points 1, 2, and 3 shown in Figure 2.

Equations of Motion

Here, we present simplified equations of motion (EoMs) describing the system behavior for all operating modes, based on the lumped-parameter approach illustrated in Figure 5 (a single-action system is illustrated for simplicity). If we consider that the fluid in the circuit is incompressible, then the combined flow of L1 and L2 is equal to the incoming

flow in the follower cylinder. When all cylinders areas are equal, it leads to the following kinematic relationship between the pistons velocities and the motor velocities:

$$v_o = v_1 + v_2 = T_1^{-1}\omega_1 + T_2^{-1}\omega_2 \tag{1}$$

where v_o , v_1 and v_2 are the linear velocity of the cylinders, ω_1 and ω_2 are the angular velocities of EM1 and EM2, and T_1 and T_2 are the transformation ratios from motor angular motion to piston linear motion, given by:

$$T_i = \frac{2\pi R_i}{\varphi_i} \tag{2}$$

where φ_i is the ball screw lead and R_i is the reduction ratio between the motor shaft and the screw. Considering the inertial properties associated with the moving parts, the passive dissipative forces and the active forces at all pistons, a 2 DoF dynamic model is constructed using the linear velocity of the output v_o and the linear velocity of L1 v_1 as state variables.

$$\mathbf{H} \begin{bmatrix} \dot{v}_o \\ \dot{v}_1 \end{bmatrix} + \underbrace{\begin{bmatrix} b_2 + b_0 \\ b_1 - b_2 \end{bmatrix}}_{\text{Disp. forces}} = \mathbf{B} \underbrace{\begin{bmatrix} I_1 \\ I_2 \end{bmatrix}}_{\text{motors}} - \underbrace{\begin{bmatrix} 0 \\ b(\phi) \end{bmatrix}}_{\text{throttling}} - \underbrace{\begin{bmatrix} f_e \\ 0 \end{bmatrix}}_{\text{ext.}} \tag{3}$$

where

$$\mathbf{H} = \begin{bmatrix} m_o + m_2 + J_2 T_2^2 & -(m_2 + J_2 T_2^2) \\ -(m_2 + J_2 T_2^2) & m_1 + J_1 T_1^2 + m_2 + J_2 T_2^2 \end{bmatrix} \tag{4}$$

$$\mathbf{B} = \begin{bmatrix} 0 & k_2 T_2 \\ k_1 T_1 & -k_2 T_2 \end{bmatrix} \tag{5}$$

with m_o , m_1 and m_2 , representing piston masses plus the inertial contribution of the transmission fluid in linear units at the piston; J_1 and J_2 represent the inertia of the motors; b_o , b_1 , and b_2 represent speed-dependent dissipative forces acting on the output, the L1 piston, and the L2 piston (friction in the seal, the ball screw, and head loss in the fluid lines), respectively; I_1 and I_2 represent the electrical currents in the motors; k_1 and k_2 represent the motor torque constants; f_e represents an external force acting on the output; and $b(\phi)$ represents a dissipative force acting on the L1 piston caused by partial closing of the ball valve. This controllable dissipative force can be modeled with:

$$b(\phi) = \frac{1}{2} \text{sgn}(v_1) k(\phi) \rho v_1^2 \frac{A_{L1}^3}{A_b^2} \tag{6}$$

where ϕ is the valve angle, A_{L1} and A_b are the bore areas of L1 and the ball valve, respectively, $k(\phi)$ an experimental mapping between the ball angle and a loss coefficient [18], and ρ is the fill fluid density.

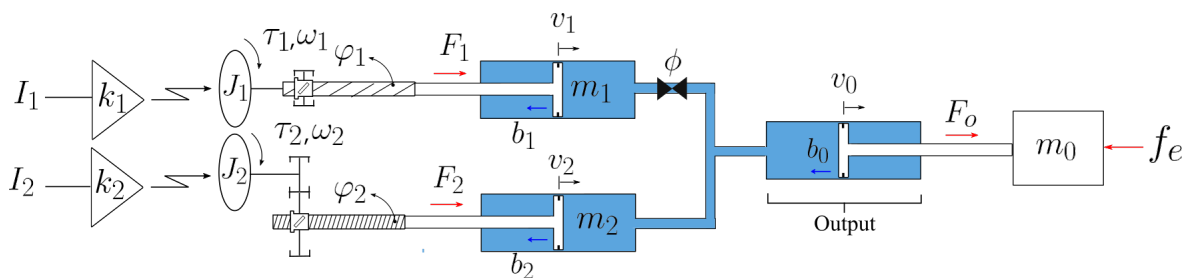


Figure 5. Model of the proposed hydrostatic architecture.

During HF mode, L1 is disconnected and no flow from L1 contributes to the output motion. Setting \dot{v}_1 to zero in (3), the model can be reduced to:

$$[m_o + \underbrace{m_2 + J_2 T_2^2}_{m_A \text{ for HF}}] \dot{v}_o + b_o + b_2 = k_2 T_2 I_2 - f_e \tag{7}$$

where m_A is the reflected inertia due to the actuation. For HS mode, both motor can contribute to the output motion. However, when isolating \dot{v}_o in (3), it can be seen that some terms related to the motion of L2 are negligible if $m_2 + J_2 T_2^2 \gg m_1 + J_1 T_1^2$ (which will be the case for the concept because T_2 is designed to be an order of magnitude greater than T_1), and the equation describing the motion of the output can be approximated by:

$$[m_o + \underbrace{m_1 + J_1 T_1^2}_{m_A \text{ for HS}}] \dot{v}_o + b_o + b_1 = k_1 T_1 I_1 - b(\phi) - f_e \tag{8}$$

All in all, with the approximation, the EoM of each mode have the same structure with the exception of an additional controllable dissipative force for HS mode. Equations show that the distinctive dynamic behavior of each mode is fundamentally due to the mechanical advantage difference between T_1 and T_2 . Indeed, in HF mode with a large T_2 , large forces can be applied (term $k_2 T_2 I_2$ in (7)) and all terms not multiplied by T_2 become negligible. The behavior is mostly a motor fighting its own internal inertia (and friction) unaffected by the load parameters and the external forces.

3. Mass and Efficiency Analysis

The proposed bimodal configuration can lead to mass and energy savings even though the design includes more components than a traditional single-motor configuration. The next section presents sets of requirements for a generic robotic knee, and a baseline actuator that are used for comparing the actuation solutions.

3.1. Two-Speed Design Advantage for a Robotic Knee

For the purpose of conducting a parametric analysis, the complex requirements of a robotic knee are simplified into three main required operating points, shown in Figure 2:

1. High-force low-speed (HF) operating point;
2. High-speed low-force (HS) operating point, with low inertia;
3. High-power braking operating point, with low inertia.

In many situations, robotic legs should feel transparent to interact with the environment/ground or with human limbs. This constraint on backdrivability is simplified into a constraint on reflected inertia from motorization. Table 1 summarizes the operating points relative to a parameter λ used as a way to scale a wide range of possible specifications.

Table 1. Robotic knee nominal parameters used for the analysis.

Operating Point i	Cont. Torque τ_i (N m)	Speed ω_i (s ⁻¹)	Inertia J_i (kg m ²)
(1) High-force (HF)	20λ	$9.4/\lambda$	-
(2) High-speed (HS)	20	9.4^*	0.07^*
(3) Braking	20λ	9.4	0.07
* Reference	-	[10]	[19]

The situation in $\lambda = 1$ describes a low-force robotic knee that is fast enough for motions like walking. Larger λ represents a knee λ times stronger but at a limited speed for less dynamic motions such as lifting a load. The output power of both HS and HF modes stays equal. λ is thus defined as the relative force ratio between the two operating modes, i.e., $\lambda = \tau_{HF} / \tau_{HS}$.

The baseline torque, speed, and inertia were selected based on human knees, exoskeletons, and prostheses: (1) 20 N m torque for a partially assisting (<50% typ.) knee exoskeleton for walking; (2) 9.4 rad/s for a human walking speed increased by a factor of 1.5 to ensure natural motion at any time; (3) 0.07 kg m² based on the low-inertia knee prosthesis design presented in [20]. The required λ ratio and exact specifications highly depend on the application. For the exoskeleton knee in [10], for sitting-to-standing and for walking, the λ is 2.8. For the legged robot in [7], for dual-speed designs for switching between the stance and swing phases of walking, λ equals 13. In the case of the knee prosthesis in [21], the λ is 5.4.

The proposed two-speed design (Figure 3) is compared with a baseline hydrostatic one (Figure 6), which inspiration is drawn from [22,23]. Mass and efficiency analyses are conducted for both designs meeting the requirements of all three operating conditions. The mass is found through the following steps: (1) computing the most advantageous reduction ratio for each configuration given the requirements, (2) computing the individual requirements (force, speed, power) of the components (cylinders, valves, ball screws, and motors) for each configuration; (3) using the scaling laws for estimating the mass of components. The approach, hypotheses, and inputs are detailed in Appendix A.

Figure 7 shows evaluated mass of the baseline and the two-speed solutions as a function of the ratio between operation points 1 and 2. The middle plot is the result for the specifications of Table 1. Note that resulting baseline masses may look high compared to state-of-the-art exoskeletons or prostheses because the calculation includes hydrostatic transmissions and cylinders, which negatively increases system weight but positively delocalize the mass in the back of the user. Many designs also do not have an inertia requirement, leading to systems feeling less transparent but having higher reduction ratios. To verify the analytical design, it can be compared with the transparent knee prosthesis in [20] which has a 57 N m continuous torque ($\lambda = 2.85$) and a 0.0696 kg.m² output reflected inertia. The authors selected a 22:1 planetary gearbox and use the frameless ILM 85 × 26 motor kit from RoboDrive, whose mass is 0.67 kg. For the same torque and inertia requirements, the modeling Equation (A4) used here finds a 22.4:1 reduction ratio and a 0.70 kg motor mass, which is relatively close to the motorization design of [20]. Their gearbox cannot be compared here since it is not a ball screw.

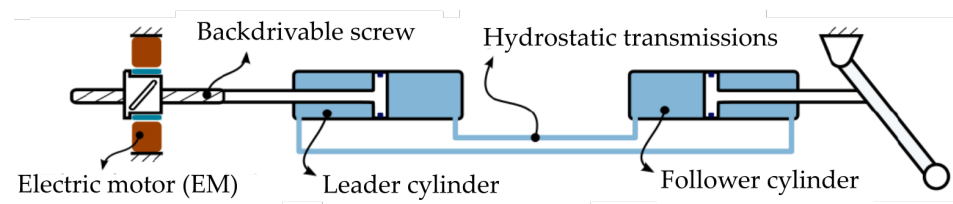


Figure 6. The baseline configuration used for analytical comparison.

If the high-force operation point is limited ($\lambda < 2.5$), then the results show that the two-speed design is not recommended due to its mass overhead from the extra components (motors, valves, pistons, ball screws). However, it is promising for high ratios ($\lambda > 2.5$), for example, for a sit-to-stand motion from a low chair for which the human knee torque is 100 N m ($\lambda = 5$) (assuming continuous torque) but at slow speeds. In this case, it would be 4.6 kg lighter than the baseline solution. The left and right plots of Figure 7 were computed to show the effect of changing the HS operating point on the results.

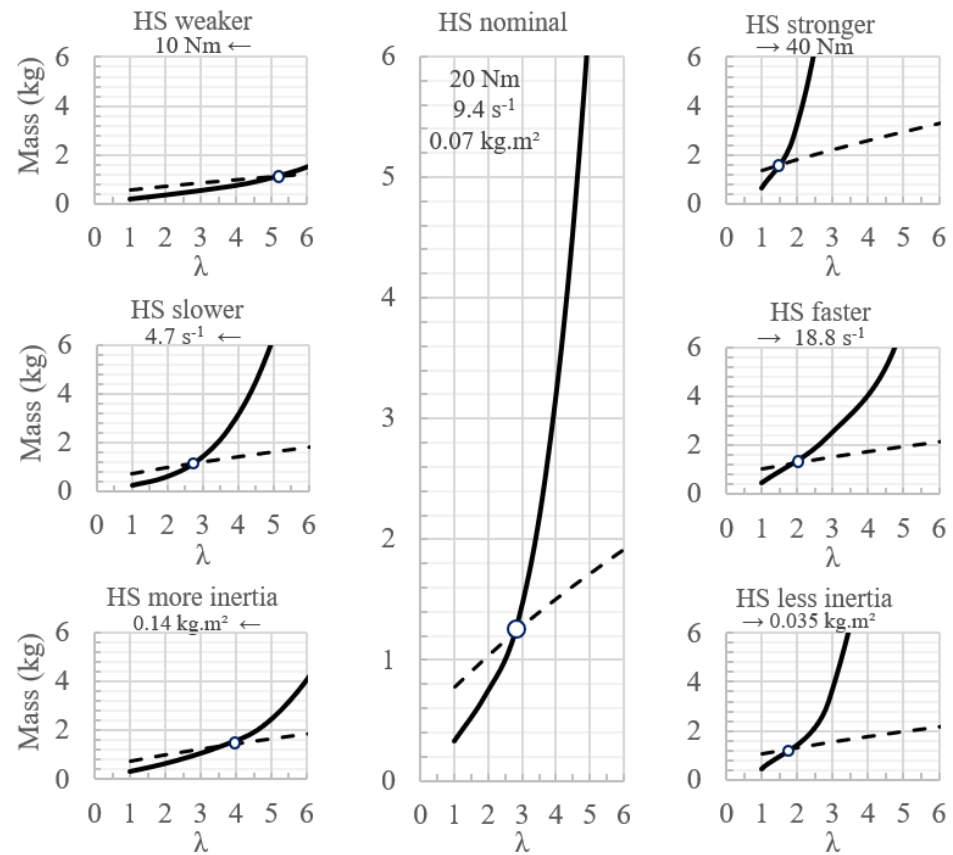


Figure 7. Predicted mass of the baseline (solid lines) and the two-speed (dashed lines) concepts. The middle curves are the analysis based on the nominal specifications. The left and right curves show the sensitivity of the mass when the high-speed mode specifications are changed.

The crossing point is sensitive to the HS mode torque and inertia because the required motor size strongly depends on the torque-to-inertia required to fulfill all operating conditions. The crossing is less sensitive to the target speed here but in other cases (which depend on the motor family and target specifications), the speed may constrain the design before the reflected inertia.

Regarding efficiency, Figure 8a,b show the results for the HF mode (a) and the HS mode (b). Joule's losses in the motor winding are scaled with motor torque and a fixed 90% ball screw efficiency is used. The motor of the baseline solution is operating at a low inefficient velocity for the HF mode. For this mode, the two-speed solution is thus more efficient. Note that in this analysis, the scaling laws are based on a very efficient (>90% at nominal torque) and low-inertia motor series (Robodrive TQ frameless motors [24]). The efficiency advantage in HF mode would be higher if using less efficient motors instead. In HS mode, the energy efficiency of each solution is similar as motors operate close to their nominal velocity but the baseline solution is slightly better since bigger motors are more efficient. Note that the energy losses due to shifting between operating modes were not modeled. Finally, Figure 8c shows the efficiency for the high-power regenerative braking condition, considering no loss at the electronics and battery. The baseline solution can actively regenerate most of the mechanical energy, whereas the two-speed solution must dissipate most of the energy through the valve.

All in all, this analysis outlines an important point: for highly strong and transparent robotics, single-ratio actuators using standard motors becomes heavy. This is where variable-speed actuators can be promising for robotics, especially regarding mass savings. For proper comparison, a designer shall include all extra components required for the variable-speed design, such as the motorized valves for the proposed actuator topology.

The next section presents the design trade-offs of custom motorized ball valves and how their mass can be estimated based on a semi-empiric equation.

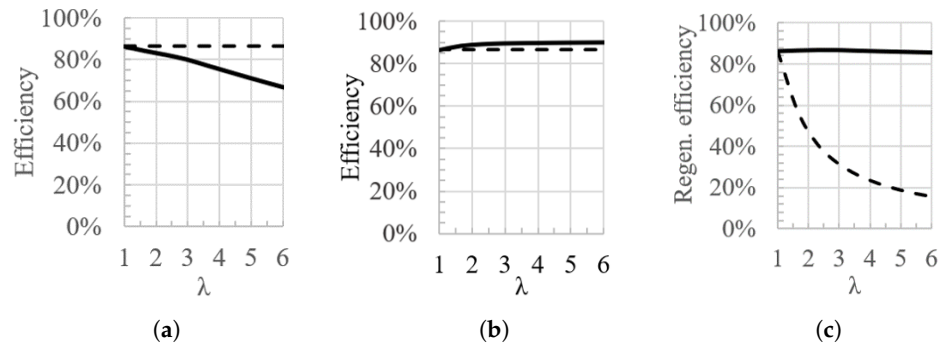


Figure 8. Efficiency comparison of the baseline configuration (solid black) with the proposed two-speed solution (dashed black). (a) High-speed mode; (b) high-force mode; (c) high-force mode.

3.2. Valve Unit

In order to meet the application requirements, the valve unit requires the following characteristics: (1) fast cycle, for tasks that require fast transitions such as between stance and swing phases of walking and running; (2) small, in terms of mass and volume; (3) low-pressure drop when fully open, for efficiency and backdrivability of the HS mode. No off-the-shelf valves are designed for such requirements.

Servo ball valves (also butterfly) are commercially available, but they are designed for industrial applications and are very heavy, cumbersome, and too slow to be used in a dynamic situation like a walking gait. Fast servo valves have been used in mobile robots for their flow modulation accuracy, high bandwidth, and lightness, for instance Boston Dynamics’s robots [25]. The main drawback of these servo valves is their inherent inefficiency and non-backdrivability since the modulation is based on restricting the flow [26]. Piloted cartridge valves have been used in digital hydraulics due to their small volume and their high speed of actuation. However, challenges remains on valve leakage and energy efficiency [27]. Solenoid type cartridge valves have been used for a long time in automobiles’ anti-lock braking systems (ABSs) [28]. The downside is that solenoids tend to be inefficient, as they required a constant supply of energy to stay open, which generates Joule’s losses, while a permanent magnet latching solenoid can mitigate this issue, it is sensitive to vibration which is inherent to dynamic systems [29]. While industrial servo ball valves are not sufficient, they demonstrated a potential use in robotic applications mainly because they are compact (with respect to the line diameter) and they exhibit a very low pressure drop when fully open [30]. An analysis is thus conducted here to determine the viability of using servo ball valves for the application, and analyzing the trade-off between the size of the valve (mass), the pressure drop when open (bore diameter), and how fast can the valve open and close (cycle time).

Equation (9) estimates the mass of a servo ball valve as a function of the desired cycle time Δt and its bore diameter d , using a semi-empiric model given by:

$$m_{\text{valve}}(d, \Delta t) = \underbrace{\frac{\pi \tau}{2\alpha \Delta t}}_{\text{motor}} + \underbrace{\frac{\tau}{\beta}}_{\text{gearbox}} + \underbrace{\frac{\rho}{Re} \left[\frac{Re}{\rho} \right]_{ref}}_{\text{body}} m_b \tag{9}$$

with

$$\tau \approx 132d - 0.2 \tag{10}$$

$$m_b \approx 41d - 0.07 \tag{11}$$

This is based on estimating individually the mass of the valve body, the electric motor actuating it and the gearbox connecting them. The mass of the electric motor is determined

by the 90° cycle time Δt , the breakaway torque τ of the valve, and the electric motors' specific power α . Furthermore, an empiric relationship between the breakaway torque and the bore diameter d based on experimental measurements on 6.35–12.7 mm commercial brass ball valves is used (Equation (10)). The model assumes conservatively that the motor must apply the breakaway torque on the whole 90° stroke. The mass of the gearbox is estimated based on a torque-to-weight ratio. Specific power α is estimated to 600 W/kg and specific torque β to 10 Nm/kg, both based on commercially available Maxon components in the range of 10–100 W. The mass of the valve body is estimated using a regression based on the valve bore diameter d (Equation (11)) using data on brass three-way ball valves (ranging from 6.35 mm to 19.05 mm) taken from the manufacturer's catalogue [31]. A ratio of material specific strength is used to predict the mass of hypothetical optimal valves made of high-strength materials. Figure 9 shows the mass prediction when using aluminum 7075. These values are only valid for valves rated at 3.45 MPa and it does not take into account the effect of increased pressure on the valve actuation torque. Tendencies show that custom servo ball valves could meet the requirements with reasonable mass. The bore diameter has more impact on the total mass than the actuation speed for a cycle time over 75 ms. According to Equation (9), this is because the gearbox and valve body have non-negligible masses and vary only with diameter. Thus, this implies that minimizing diameter will have a more noticeable effect on mass reduction than trying to be conservative on actuation speed. However, for the same flow rate, designers should consider that viscous friction head losses increase by a factor of d^{-5} , which can be problematic.

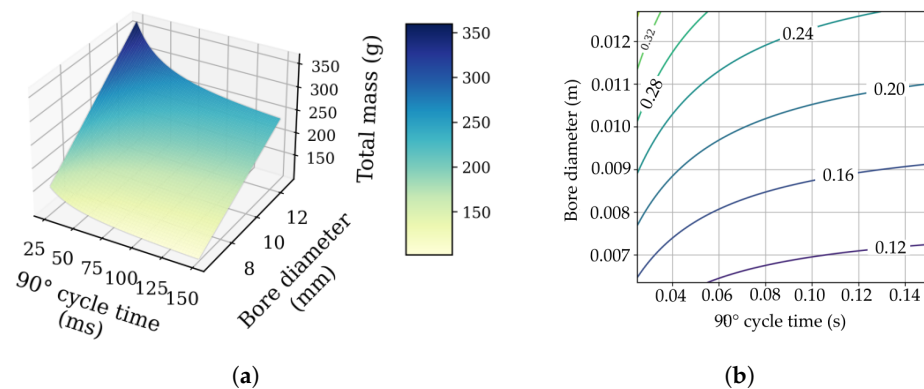


Figure 9. Mass mapping for aluminum motorized ball valves as a function of the bore diameter and 90° cycle time: (a) 3D view of the map; (b) 2D view of the map.

4. Experimental Assessment

This section presents the experimental analysis of a custom actuation system and a robotic leg test bench.

4.1. Prototypes and Test Bench

A prototype of two servo-actuated ball valves was designed and built, as shown in Figure 10a. Standard brass T-pattern flow 3-way ball valves (Valworx, 536903, Cornelius, NC, USA) were used and each valve is driven by a high torque servo motor (Savox, SB2262SG, Salt Lake City, UT, USA), through a custom single stage of spur gears for faster switching (1:1.33). The servo motor was chosen for its high torque (3.2 Nm), speed ($16 \text{ rad}\cdot\text{s}^{-1}$), and small volume ($41 \times 20 \times 26 \text{ mm}$).

The mass of the valve unit prototype is 415 g and it reaches a maximum speed of $12.2 \text{ rad}\cdot\text{s}^{-1}$ (130 ms of cycle time). In comparison, for brass, Equation (9) predicts 447 g (including printed components) which is 8% more than the prototype. This corresponds to a mass reduction of 82% compared to equivalent commercial motorized valves [32] and it could be optimized. Indeed, as shown in Figure 10c, the valve body accounts for 52% of the total valve mass. By choosing a light body material such as aluminum, Equation (9)

predicts a mass of 172 g for an equivalent unit (9.52 mm bore, 0.130 s cycle time). In this case, the total mass reduction would be 93% compared to commercial motorized valves.

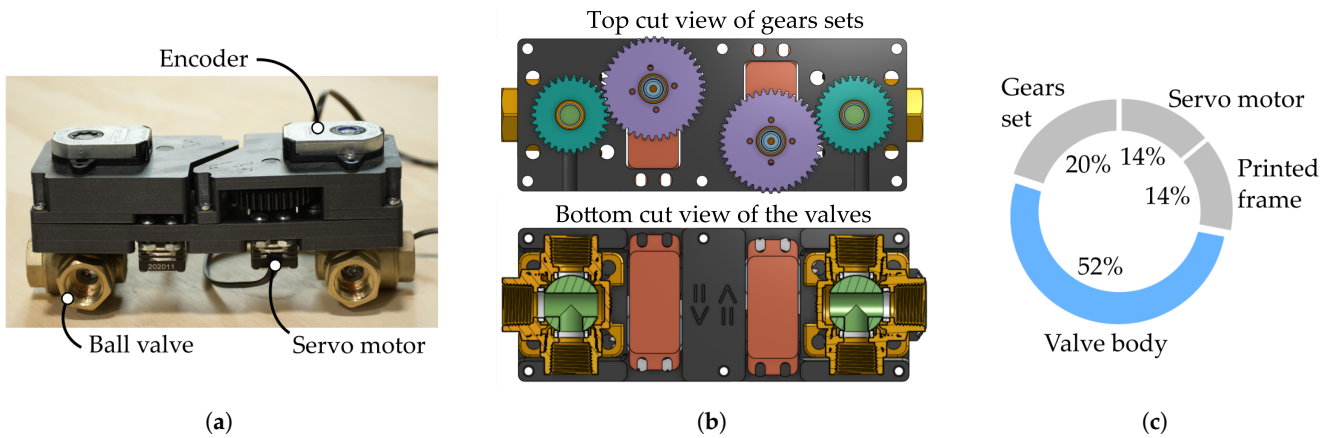


Figure 10. Motorized valve unit prototype built with two commercial three-way ball valves and servo motors. (a) Actual prototype overview; (b) top and bottom cut views; (c) mass distribution.

The complete two-speed concept was built using custom valve unit and commercially available components as shown in Figure 11.

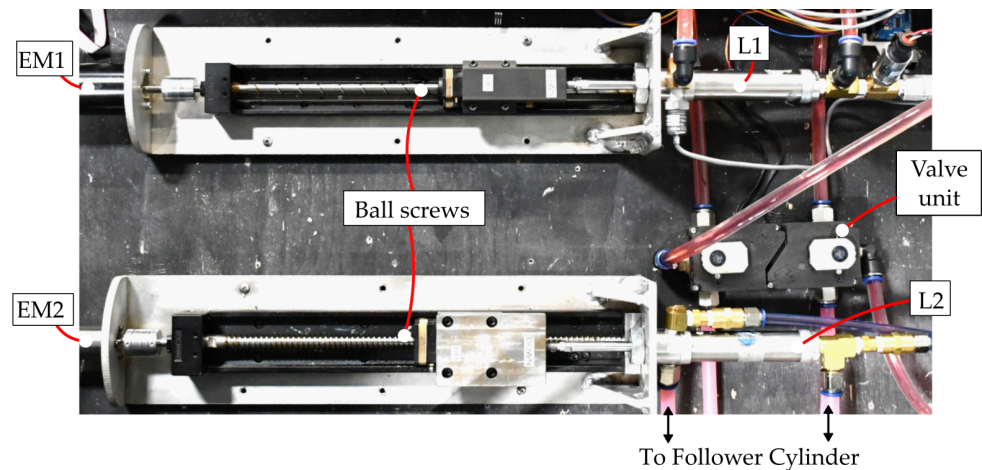


Figure 11. Hydrostatic actuator components layout.

One 200 W nominal motor (Maxon RE50, Sachseln, Switzerland, operated up to $2.6\times$ the nominal current) and one 102 W nominal motor (Maxon DCX32L, Sachseln, Switzerland) are used for EM1 and EM2, respectively. EM1 is coupled to a 20 mm ball screw lead (NSK MCM05025H20K00, Tokyo, Japan) while EM2 is coupled to a 5 mm ball screw lead (NSK MCM06025H05K02, Tokyo, Japan) through a 28:1 planetary gear head (Maxon GPX32, Sachseln, Switzerland). Hydraulic cylinders (Bimba H-093-DUZ, University Park, IL, USA, rated 3.45 MPa) are used and equipped with pressure sensors (Measurement Specialties, MSP300, Hampton, USA). Propylene glycol is used as the transmission fluid for its non-toxicity, low viscosity, and anti-corrosive properties. The prototype actuates a custom robotic leg test bench shown in Figure 4. The robot main links are made of thick carbon fiber tubes. The tibia link is 483 mm long with a 26.6 mm outside diameter tube that is 2.5 mm thick. The femur link is 394 mm long with a 43.5 mm outside diameter tube that is 3.4 mm thick. The robotic leg is attached to a cart (where steel plates can be installed as a payload) fixed to vertical linear guides. The bidirectional actuation of the knee can either swing the leg in the air, when the cart rests on the bottom of the linear guide, or lift the cart and payload vertically when the foot touches the ground. The hip joint of the leg is deactivated. The prototype capabilities are shown graphically on Figure 12.

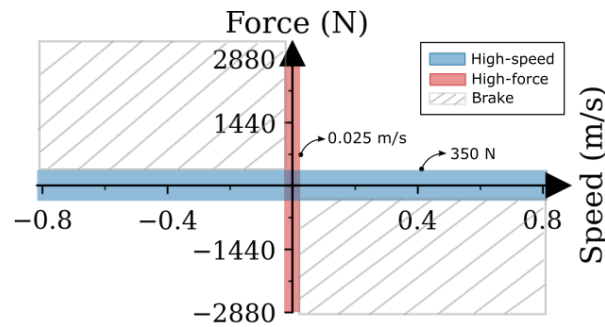


Figure 12. Bimodal system operating regions in terms of force and speed.

The maximum generated output force, using the maximum motor currents, is 350 N in HS mode and 2880 N in HF mode, which means the leg can sustain a payload of about 7.6 kg in HS mode and about 62 kg in HF mode. The maximum theoretical speed limit based on $T_i^{-1}w_i$ with the maximum motors velocities are 0.8 m s^{-1} in HS and 0.025 m s^{-1} in HF.

4.2. Control Architecture

Three elements are controlled on the actuator: EM1, EM2, and the valve unit. EM1 is current controlled, which is closely related to the generated output pressure, since this line has a small reduction ratio whereas EM2 is speed controlled since it fights its own internal inertia and friction due to the large reduction ratio. The valve is controlled by imposing its position with the servo motor using its internal closed loop. Figure 13 summarizes the control scheme proposed to handle the different operating modes.

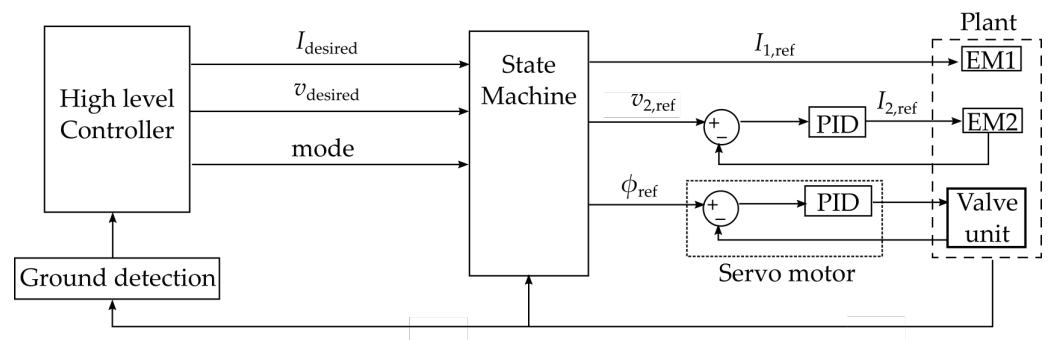


Figure 13. Actuator control structure based on state machine and PID controllers.

Here, since the two valves move simultaneously for all transitions, only one variable is shown for simplicity. A high-level controller specifies the mode and a reference (current in HS and velocity in HF) to a state machine. For demonstrating the capabilities of the actuator, the high-level controller is a hard-coded sequence of motion, with the exception of the downshift transition that is triggered by a ground contact detection using a combination of conditions on the knee joint encoder signal and the pressure signal in the follower cylinder.

4.3. State Machine and Transitions

Achieving smooth transitions when changing modes in dynamic situations is not trivial. For a robotic leg, when it hits the ground in HS mode, the total force generated at the output cylinder needs to be maintained, otherwise the leg may collapse. Furthermore, during that period, there is a transition time where the output force and speed are subjected to fluctuations due to the closing of the valves. Hence, valve tests are conducted to find good control strategies between operating modes. Linear positions and velocities are displayed since the measurements are taken directly at the pistons. For this purpose, Figure 14 shows the effect of closing the valves on the output speed and on the calculated dissipative force using the prototypes of Section 4.

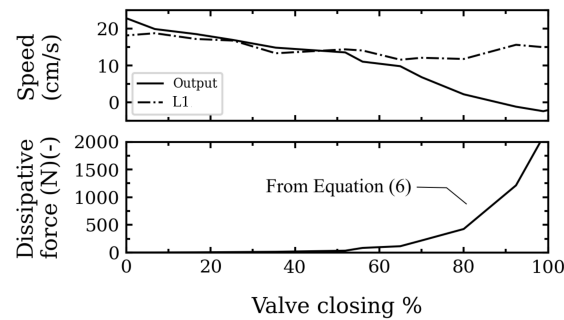


Figure 14. Contribution of leader cylinder (L1) on the total output speed (top) and theoretical dissipative force (bottom) when closing the valves.

The robotic leg is held so it does not come into contact with the ground during the sequence. Between 0% and 50% valve closure, the output speed and L1 speed are directly correlated and the dissipative force is negligible. However, at 50% valve closure, L1 loses its authority: its speed stays constant while the output speed starts decreasing. This behavior can be explained by the generated dissipative force, which starts to increase exponentially, as predicted through Equation (6). Around 90% valve closure, the output speed reaches zero, meaning that from this value, the local losses are sufficiently high to block the contribution of L1. Hence, these observations suggest that EM1 should provide a continuous torque until at least 50% valve closure in order to provide initial payload support before EM2 can generate sufficient force at the output. Finally, between 90% and 100%, the output speed becomes negative, which can cause oscillations.

To minimize these oscillations, three control strategies are compared during a downshift sequence, as shown in Figure 15.

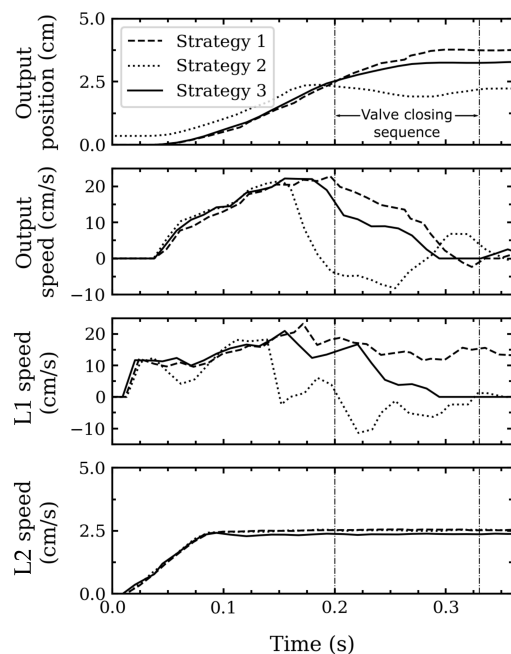


Figure 15. Comparison of three switching strategies for a downshift.

Each sequence starts in HS mode, where both L1 and L2 contribute to the output speed. Then, at 0.2 s, the valve closing sequence is initiated. Finally, at 0.33 s, the downshift is completed and the sequence ends in HF mode. Strategy 1 consists of keeping L1 speed constant during the entire valve closing sequence. Strategies 2 and 3 both consist of reducing L1 speed before the end of the valve closing sequence. However, the former uses

a speed command while the latter uses a current command. Looking at the output speed, strategy 1 causes slight negative value at the end of the closing sequence. As for strategy 2, the output speed fluctuates, which translates into worse performance. Finally, strategy 3 shows the best performance since the output speed slows rapidly before the end of the closing sequence. By looking at the position, it enables a smooth downshift in less distance and without oscillations. The switching conditions are detailed in Figure 16.

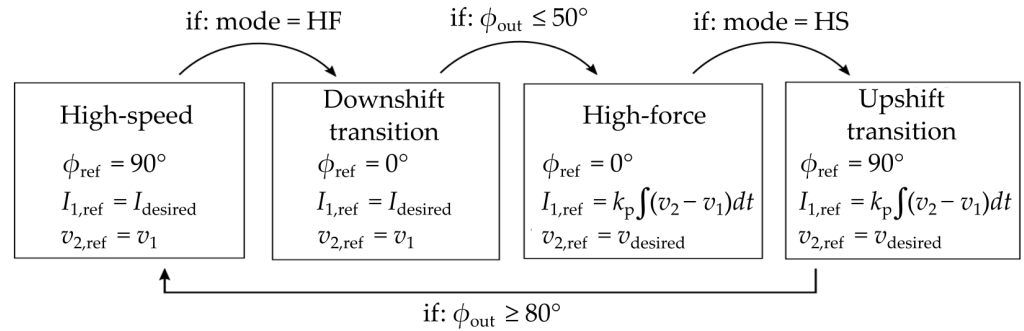


Figure 16. State machine of the controller.

Following calibration tests, the optimal conditions on the position of the valve necessary for a change of control of the motors for a downshift and an upshift were set at 50° and 80° , respectively. Note that, due to stroke limitations, it is desirable to have both leader cylinders stroke as close as possible to the follower cylinder stroke. Thus, in HF mode, EM1 is commanded to follow L2 position and vice versa in HS mode.

4.4. Experimental Results for Controlling a Robotic Knee

The two-speed hydrostatic principle is tested here by addressing the transitions between the HS and HF modes upon contact with the ground as well as the braking capabilities. The tests have been visualized in the video S1 attached to the paper.

4.4.1. Downshift and Upshift Between HS and HF Modes

Figure 17 illustrates a test sequence analogous to a complete gait cycle: starting from rest, the leg first swings at high-speed in HS mode (a) then the foot hits the ground at high speed. The actuator detects this impact and downshifts in HF mode by closing the valves (b). Then, the leg moves up then down, lifting a 10 kg payload (c). Finally, valves are opened (d) to allow the leg to be retracted quickly using the HS mode (e). Control signals from the experiments are shown at Figure 18. Note that the net output force signal (at output cylinder) is derived from the localized pressure sensor.

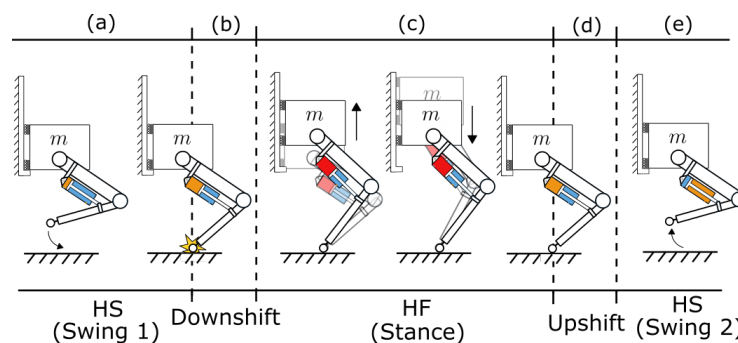


Figure 17. Motion sequence for the downshift and upshift transition test. The labels (a) to (e) are described in the text.

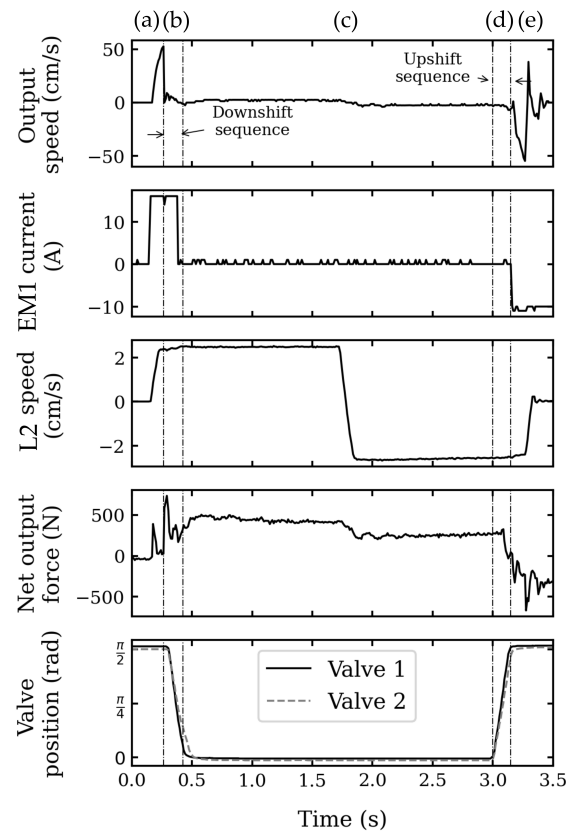


Figure 18. Results for the downshift and upshift transition test under load. The labels (a) to (e) are described in the text.

Results show pressure oscillations that lead to observable second order behaviors. Before ground contact (swing acceleration), the first resonant peak of force (400 N) reveals the compliance of the transmission, neglected in the model and coupled to the inertia of the leg. Then, a second peak of external force (730 N) occurs at the impact with the ground again due to the transmission compliance and the sudden deceleration of the motor inertia. Without anticipation of this impact, this peak force cannot be mitigated easily by control but the low actuation and robot inertia minimize these effects. Furthermore, it can be seen that, during the downshift process, the output force does not drop and is maintained around 300 N, the capability of HS mode, until the valves are fully closed and EM2 can start bearing the whole weight. The downshift and upshift are conducted in about 0.130 s.

4.4.2. Throttling the Valve for High Braking Forces

Here, it is demonstrated that the valve itself can be used to create large braking forces (in quadrants II and IV; see Figure 12) during HS mode. Figure 19 shows the motion sequence analogous to a landing. Starting 0.25 m above ground with valves halfway closed (constant 45° position) (a), the robotic leg is dropped. Upon ground contact, energy is dissipated by the valves generating high braking force (b). Then, the carriage reaches the stopper and the systems comes at rest (c). Figure 20 shows that a braking force over 1500 N was generated at a high velocity during HS mode by throttling the ball valve, using the dissipative force $b(\phi)$ shown in Equation (3). The robot is dropped with a total payload of 17 kg, including leg mass. The peak braking power here is 960 W, which is largely over the maximal power of HS and HF modes. Using $k(\phi)$ and Equation (6), it would be possible to dissipate even more energy by throttling the valve dynamically.

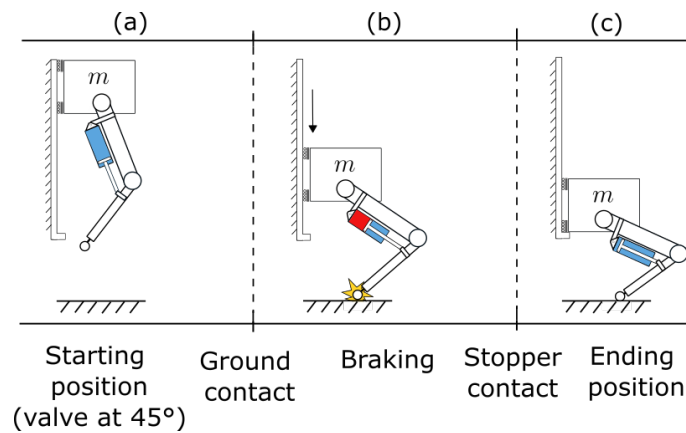


Figure 19. Motion sequence for the landing test. The labels (a) to (c) are described in the text.

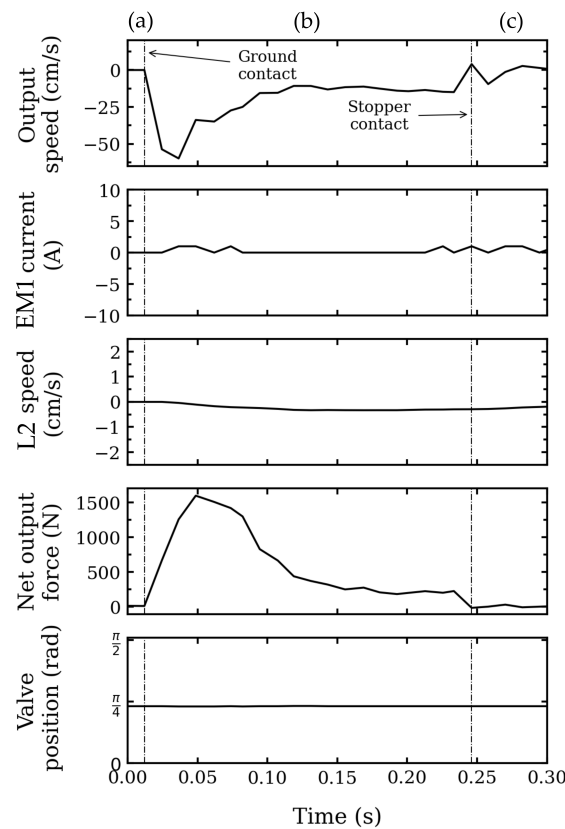


Figure 20. Drop test sequence showcasing the brake capacity of the valve when positioned at 45° . The labels (a) to (c) are described in the text.

5. Conclusions

In this paper, a novel bimodal hydrostatic architecture that uses motorized ball valves to dynamically reconfigure the system between two operating modes of a robotic leg is presented. First, the working principle and equations of motion for the hydrostatic architecture are detailed. Then, potential gains in terms of mass and energy saving of the hydrostatic two-speed design were analyzed for three operation points and a custom switching valve unit is presented with an insight on the design trade-offs between the mass, delay, and flow. Control strategies for upshift and downshift are detailed and tested on a robotic leg prototype having completed a sequence similar to a walking gait. At last, the high braking capabilities of the valves are demonstrated.

In the context of a knee exoskeleton, compared to a baseline configuration using one motor, mass analyses show that a two-speed solution is promising when high force is

necessary. Furthermore, the two-speed architecture proved to be more efficient in HF mode. Experimental results show that (1) motorized ball valves can make transition between operating modes; (2) the proposed operating principle and control schemes allow for the actuator to maintain a constant force during transition after an impact with the ground; (3) the proposed actuator topology can meet the needs of a leg bimodal operation in terms of force, speed, and compliance.

The bimodal actuation of a robotic system using motorized ball valves is possible and is to be considered for switching between tasks (e.g., between slow lifting and walking). For switching within a task (e.g., between stance and swing phases), in terms of cycle time, it is not clear if the actual motorized valve prototype would be fast enough. Still, its simplicity in terms of downshift and upshift control and its ability to maintain forces during transitions show potential compared to previous developed solutions, where specific conditions and additional components were required to shift. The general concept presented and tested could be applied to any system other than a robotic leg. However, many aspects of using bimodal hydrostatic architecture still need to be addressed. In terms of the proposed architecture, an optimized design of the proposed actuator, including the valve unit, is yet to be developed to prove that it is really suitable to embedded mobile robotic legs. Finally, transition control could be fine-tuned based on pressure signals and force transmitted.

Supplementary Materials: The following supporting information can be downloaded at: <https://www.mdpi.com/article/10.3390/act12120452/s1>, Video S1: A Bimodal Hydrostatic Actuator for Robotic Legs with Compliant Fast Motion and High Lifting Force.

Author Contributions: Conceptualization, A.L., J.D., J.-S.P. and A.G.; methodology, A.L., J.D., J.-S.P., and A.G.; software, A.L.; validation, A.L.; formal analysis, A.L. and J.D.; investigation, A.L.; resources, A.L.; data curation, A.L.; writing—original draft preparation, A.L. and J.D.; writing—review and editing, A.L., J.D., J.-S.P. and A.G.; visualization, A.L.; supervision, A.G. and J.-S.P.; project administration: A.G.; funding acquisition, A.G. All authors have read and agreed to the published version of the manuscript.

Funding: This work was funded by the Fonds Québécois de la Recherche sur la Nature et les Technologies (FRQNT) (2021-NC-285727) and the Natural Sciences and Engineering Research Council of Canada (NSERC).

Data Availability Statement: The data presented in this study are available on request from the author.

Conflicts of Interest: The authors declare no conflicts of interest. The funders had no role in the design of the study; in the collection, analyses, or interpretation of data; in the writing of the manuscript; or in the decision to publish the results.

Abbreviations

The following abbreviations are used in this manuscript:

EM	electric motor
L	leader (piston/cylinder)
HS	high speed
HF	high force

Appendix A. Mass Modeling Using Scaling Laws

This section presents the mass modeling of the main components in the designs. Their properties are scaled using scaling laws which give a general trend of the main properties y of system components based on geometric and materials similarity. The form is given by $y = kx^a$, where the reference parameter is x and the scaling parameters are k and a . Scaling laws were used for simplified design purposes just like in [3,33,34]. Scaling parameters are summarized in Table A1 with details in the next subsections.

Table A1. Scaling law parameters used for modeling, $y = kx^a$.

Component and Property y	Scaled from x	k	a	Units	Ref.
Electric motor (M)	τ_M			N m	[24]
Mass		0.25	0.99	kg	[35]
Nominal speed		487	-0.54	s^{-1}	
Rotor inertia		3.06×10^{-5}	1.46		
Joule's coeff.		17.6	-1.62	W/Nm^2	
Diameter OD		0.07	0.235	m	
Ball screw (BS)	F_{BS}			N	[36]
Force density		15,000	0	$N kg^{-1}$	
Hydraulic cylinder	$F_{cyl.}$			N	[37]
Force density		977	0.26	$N kg^{-1}$	

(1) *Reduction ratio selection:* The selection of the best reduction ratio N for an application depends on the desired torque, speed and reflected inertia from the gear motor. Inertia is amplified by N^2 through the transmission, $J_i = J_M N^2$. Then, the maximum ratio is either limited by motor inertia J_M or by motor nominal speed ω_M :

$$N = \min \left\{ \begin{array}{l} \sqrt{J_i / J_M} \\ \omega_M / \omega_i \end{array} \right. \tag{A1}$$

$$\tau_M = \tau_i / (\eta_{BS} N) \tag{A2}$$

where J_M and ω_M are scaling functions from Table A1 depending on motor torque τ_M which also depends on N , on the transmission efficiency and on the joint torque. From Equations (A1) and (A2), the unknowns N and τ_M can be found from the output torque, speed, and inertia requirements.

(2) *Motors:* When coupled with lightly geared transmissions, brushless DC in-runner motors with large diameters are torque-dense with reasonable reflected inertia [3]. In this paper, the 48 V frameless torque motor series from TQ Systems is used as a reference (ILM and ILM-E series) [24,35]. The scaling laws found are plotted in Figure A1 as an example. For each model, the winding that allows the maximum speed was used. Joule's losses are at 25 °C and would be 30% higher at 100 °C. Iron losses (proportional to speed) are neglected.

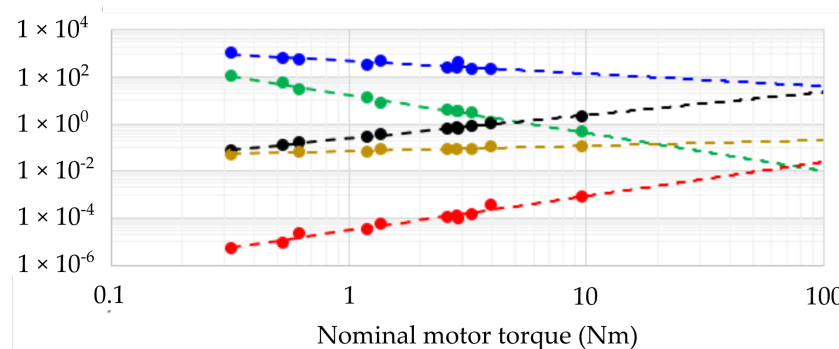


Figure A1. Scaling laws found for the TQ Systems motor family used with extrapolation up to 100 N m: mass (kg) in black, nominal speed (s^{-1}) in blue, rotor inertia ($kg m^2$) in red, Joule's coefficient (W/Nm^2) in green, and outside diameter (m) in yellow.

(3) *Ball screws:* Ball screws are torque dense rotational-to-linear mechanisms with high forward and reverse efficiency ($\eta_{BS} > 90\%$ for lead angles higher than 5°) [36,38]. For scaling small stroke assemblies, screw and nut mass must be considered, as well as extra screw length due to the nut. Scaling laws were fit on NSK ball screws (RNFTL model, [36]) for a 100 mm stroke. The total force density found is about constant with $15 kN kg^{-1}$ for a 0.5–15 kN range.

(4) *Hydraulic Cylinders*: For same work per stroke, high-pressure cylinders are lighter and less flow is required, so smaller hoses can be used. The LCS series from KNR Robotics is selected. Their force-to-weight ratio is given for a $\Delta x_{\text{cyl.}} = 100$ mm linear stroke [37] and we fit a scaling law on it. For a maximum 160° angular stroke for the knee [10], a $R_{\text{eff.}} = 36$ mm effective radius of action is thus required. The required cylinder force is thus given by Equation (A3)

$$F_{\text{cyl.}} = \frac{\tau_i R_{\text{eff.}}}{\Delta x_{\text{cyl.}}} \quad (\text{A3})$$

The scaling law from Table A1 is then used to find the cylinders mass based on this required force.

(5) *Motorized ball valves*: The mass m_{valve} of the two motorized ball valves for the two-speed design is based on Equations (9)–(11). For an 8 mm diameter valve and a 100 ms switching time, the mass is 0.14 kg each.

(6) *Example*: A baseline power unit mass calculation is given here as an example. For $\lambda = 4$, the target speed and torque are 9.4 rad/s and 80 Nm, respectively. Based on Table A1 parameters and Equations (A1) and (A2), the maximum reduction ratio is 9 for the inertia and 27 for the speed, so $N = 9$ and $\tau_M = (80 \text{ Nm}) / ((0.9)(9)) = 9.9 \text{ Nm}$. Furthermore, Equation (A3) gives a 2230 N cylinder force $F_{\text{cyl.}}$ and ball screw force F_{BS} . The total power unit mass is then:

$$m_{\text{tot.}} = \underbrace{k_M \tau_M^{a_M}}_{\text{motor}} + \underbrace{\frac{F_{\text{BS}}}{k_{\text{BS}} F_{\text{BS}}^{a_{\text{BS}}}}}_{\text{ball screw}} + \underbrace{\frac{2F_{\text{cyl.}}}{k_{\text{cyl.}} F_{\text{cyl.}}^{a_{\text{cyl.}}}}}_{\text{cylinders}} \quad (\text{A4})$$

$$m_{\text{tot.}} = \underbrace{0.25(9.9)^{0.99}}_{\text{motor}} + \underbrace{\frac{2230}{15000(2230)^0}}_{\text{ball screw}} + \underbrace{\frac{2(2230)}{977(2230)^{0.26}}}_{\text{cylinders}} \quad (\text{A5})$$

The total mass is $m_{\text{tot.}} = 2.4 + 0.15 + 2(0.31) = 3.17$ kg.

References

1. Sarcos Robotics. Expanding the Limits of Human Potential—Guardian XO. Available online: <https://www.sarcos.com/products/guardian-xo-powered-exoskeleton/> (accessed on 19 May 2023)
2. Panizzolo, F.A.; Galiana, I.; Asbeck, A.T.; Sivi, C.; Schmidt, K.; Holt, K.G.; Walsh, C.J. A biologically-inspired multi-joint soft exosuit that can reduce the energy cost of loaded walking. *J. Neuroeng. Rehabil.* **2016**, *13*, 43. [CrossRef] [PubMed]
3. Seok, S.; Wang, A.; Otten, D.; Kim, S. Actuator design for high force proprioceptive control in fast legged locomotion. In Proceedings of the 2012 IEEE/RSJ International Conference on Intelligent Robots and Systems, Vilamoura-Algarve, Portugal, 7–12 October 2012; pp. 1970–1975. [CrossRef]
4. Bledt, G.; Powell, M.J.; Katz, B.; Di Carlo, J.; Wensing, P.M.; Kim, S. MIT Cheetah 3: Design and Control of a Robust, Dynamic Quadruped Robot. In Proceedings of the 2018 IEEE/RSJ International Conference on Intelligent Robots and Systems (IROS), Madrid, Spain, 1–5 October 2018; pp. 2245–2252. [CrossRef]
5. Girard, A.; Asada, H.H. A two-speed actuator for robotics with fast seamless gear shifting. In Proceedings of the 2015 IEEE/RSJ International Conference on Intelligent Robots and Systems (IROS), Hamburg, Germany, 28 September–2 October 2015; pp. 4704–4711. [CrossRef]
6. He, J.; Gao, F. Mechanism, Actuation, Perception, and Control of Highly Dynamic Multilegged Robots: A Review. *Chin. J. Mech. Eng.* **2020**, *33*, 79. [CrossRef]
7. Hirose, S.; Yoneda, K.; Arai, K.; Ibe, T. Design of prismatic quadruped walking vehicle TITAN VI. In Proceedings of the Fifth International Conference on Advanced Robotics 'Robots in Unstructured Environments, Pisa, Italy, 19–22 June 1991; Volume 1, pp. 723–728. [CrossRef]
8. Bell, J.H. A Two-Motor Actuator for Legged Robotics Applications. Ph.D. Thesis, Massachusetts Institute of Technology, Cambridge, MA, USA, 2020.
9. Jeong, S.H.; Kim, K.S. A 2-Speed Small Transmission Mechanism Based on Twisted String Actuation and a Dog Clutch. *IEEE Robot. Autom. Lett.* **2018**, *3*, 1338–1345. [CrossRef]
10. Lee, Y.; Lee, J.; Choi, B.; Lee, M.; Roh, S.g.; Kim, K.; Seo, K.; Kim, Y.J.; Shim, Y. Flexible Gait Enhancing Mechatronics System for Lower Limb Assistance (GEMS L-Type). *IEEE/ASME Trans. Mechatron.* **2019**, *24*, 1520–1531. [CrossRef]

11. Kim, B.-S.; Song, J.-B.; Park, J.-J. A Serial-Type Dual Actuator Unit With Planetary Gear Train: Basic Design and Applications. *IEEE/ASME Trans. Mechatron.* **2010**, *15*, 108–116. [CrossRef]
12. Verstraten, T.; Furnémont, R.; López-García, P.; Rodríguez-Cianca, D.; Vanderborght, B.; Lefeber, D. Kinematically redundant actuators, a solution for conflicting torque–speed requirements. *Int. J. Robot. Res.* **2019**, *38*, 612–629. [CrossRef]
13. Girard, A. Fast and Strong Lightweight Robots Based on Variable Gear Ratio Actuators and Control Algorithms Leveraging the Natural Dynamics. Ph.D. Thesis, Massachusetts Institute of Technology, Cambridge, MA, USA, 2017.
14. Khazoom, C.; Veronneau, C.; Bigue, J.P.L.; Grenier, J.; Girard, A.; Plante, J.S. Design and Control of a Multifunctional Ankle Exoskeleton Powered by Magnetorheological Actuators to Assist Walking, Jumping, and Landing. *IEEE Robot. Autom. Lett.* **2019**, *4*, 3083–3090. [CrossRef]
15. Whitney, J.P.; Chen, T.; Mars, J.; Hodgins, J.K. A hybrid hydrostatic transmission and human-safe haptic telepresence robot. In Proceedings of the 2016 IEEE International Conference on Robotics and Automation (ICRA), Stockholm, Sweden, 16–21 May 2016; pp. 690–695. [CrossRef]
16. Sugihara, K.; Nozaki, T.; Murakami, T. Continuously Variable Transmission by High-speed Path Switching of Linear Electrohydrostatic Actuator. In Proceedings of the IECON 2019—45th Annual Conference of the IEEE Industrial Electronics Society, Lisbon, Portugal, 14–17 October 2019; Volume 1, pp. 3603–3608. [CrossRef]
17. Denis, J.; Lecavalier, A.; Plante, J.S.; Girard, A. Multimodal Hydrostatic Actuators for Wearable Robots: A Preliminary Assessment of Mass-Saving and Energy-Efficiency Opportunities. In Proceedings of the 2022 International Conference on Robotics and Automation (ICRA), Philadelphia, PA, USA, 23–27 May 2022; pp. 8112–8118. [CrossRef]
18. Ozdamar, A.; Gursel, K.T.; Pekbey, Y.; Celikag, B. An Experimental and Numerical Study on Pressure Drop Coefficient of Ball Valves. *Int. Energy J.* **2007**, *8*, 301–308.
19. Ramachandran, H.; Vasudevan, D.; Brahma, A.; Pugazhenthii, S. Estimation of mass moment of inertia of human body, when bending forward, for the design of a self-transfer robotic facility. *J. Eng. Sci. Technol.* **2016**, *11*, 166–176.
20. Elery, T.; Rezazadeh, S.; Nesler, C.; Gregg, R.D. Design and Validation of a Powered Knee–Ankle Prosthesis with High-Torque, Low-Impedance Actuators. *IEEE Trans. Robot.* **2020**, *36*, 1649–1668. [CrossRef] [PubMed]
21. Culver, S.C.; Vailati, L.G.; Goldfarb, M. A Primarily-Passive Knee Prosthesis with Powered Stance and Swing Assistance. In Proceedings of the 2022 International Conference on Rehabilitation Robotics (ICORR), Rotterdam, The Netherlands, 25–29 July 2022; pp. 1–6. [CrossRef]
22. Veronneau, C.; Denis, J.; Lebel, L.P.; Denninger, M.; Blanchard, V.; Girard, A.; Plante, J.S. Multifunctional Remotely Actuated 3-DOF Supernumerary Robotic Arm Based on Magnetorheological Clutches and Hydrostatic Transmission Lines. *IEEE Robot. Autom. Lett.* **2020**, *5*, 2546–2553. [CrossRef]
23. Carney, M.E.; Shu, T.; Stolyarov, R.; Duval, J.F.; Herr, H.M. Design and Preliminary Results of a Reaction Force Series Elastic Actuator for Bionic Knee and Ankle Prostheses. *IEEE Trans. Med. Robot. Bionics* **2021**, *3*, 542–553. [CrossRef]
24. TQ Systems. ILM Series Framesless Servo Kits. Available online: https://www.tq-group.com/filedownloads/files/products/robodrive/data-sheets/en/DRVA_DB_Servo-Kits_ILM_EN_Rev408_Web.pdf (accessed on 19 May 2023).
25. Gizzo, E.; Ackerman, E. Boston Dynamics’ Marc Raibert on Next-Gen ATLAS: “A Huge Amount of Work”. In *IEEE Spectrum*; IEEE: Piscataway, NJ, USA, 2016.
26. Buerger, S.P.; Hogan, N. Novel Actuation Methods for High Force Haptics. In *Advances in Haptics*; InTech: London, UK, 2010; p. 33. [CrossRef]
27. Lantela, T.; Pietola, M. High-flow rate miniature digital valve system. *Int. J. Fluid Power* **2017**, *18*, 188–195. [CrossRef]
28. Linjama, M. Digital fluid power—State of the art. In Proceedings of the Twelfth Scandinavian International Conference on Fluid Power, Tampere, Finland, 18–20 May 2011; Volume 12, p. 23.
29. Solutions, S. Latching Solenoid Valves Low Energy. 2021. Available online: <https://www.solenoidsolutionsinc.com/specialty-valves/latching-solenoid-valves-low-energy/> (accessed on 19 May 2023).
30. Hashemi, S.; Mitchell, H.; Durfee, W.K. Experimentally validated models for switching energy of low pressure drop digital valves for lightweight portable hydraulic robots. In Proceedings of the ASME/BATH 2019 Symposium on Fluid Power and Motion Control, FPMC 2019, Longboat Key, FL, USA, 7–9 October 2019. [CrossRef]
31. Valworx. 5368/5369 Series Full Port Lead Free Brass 3-Way Ball Valves. Available online: <http://cdn.valworx.com/downloads/datasheets/valworx/53685369.pdf> (accessed on 19th May 2023).
32. Valworx. 5679 Series Electric Actuated 3-Way Ball Valves Product Data Sheet. Available online: <https://s3.amazonaws.com/cdn.valworx.com/downloads/datasheets/valworx/5679.pdf> (accessed on 19 May 2023).
33. Budinger, M.; Liscouët, J.; Hospital, F.; Maré, J.C. Estimation models for the preliminary design of electromechanical actuators. *Proc. Inst. Mech. Eng. Part G J. Aerosp. Eng.* **2012**, *226*, 243–259. [CrossRef]
34. Saerens, E.; Crispel, S.; Garcia, P.L.; Ducastel, V.; Beckers, J.; De Winter, J.; Furnémont, R.; Vanderborght, B.; Verstraten, T.; Lefeber, D. Scaling laws for parallel motor-gearbox arrangements. In Proceedings of the 2020 IEEE/RSJ International Conference on Intelligent Robots and Systems (IROS), Las Vegas, NV, USA, 24 October 2020–24 January 2021; pp. 6339–6346. [CrossRef]
35. TQ Systems. ILM-E Series Frameless Servo Kits. Available online: https://www.tq-group.com/filedownloads/files/products/robodrive/data-sheets/en/DRVA_DB_Servo-Kits_ILM-E_EN_Rev102_Web.pdf (accessed on 19 May 2023).
36. NSK. NSK Precision Machine Components—Ball Screws, 2013. Available online: https://stevenengineering.com/Tech_Support/PDFs/NSK-HB_BALL-SCREWS.pdf (accessed on 19 May 2023).

37. KNR Systems Inc. *Hydraulic Actuator—RH/LH Series*; KNR Systems Inc.: Yongin-si, Republic of Korea.
38. THK. Features of the Ball Screws. Available online: https://tech.thk.com/en/products/pdf/en_b15_006.pdf (accessed on 19 May 2023).

Disclaimer/Publisher’s Note: The statements, opinions and data contained in all publications are solely those of the individual author(s) and contributor(s) and not of MDPI and/or the editor(s). MDPI and/or the editor(s) disclaim responsibility for any injury to people or property resulting from any ideas, methods, instructions or products referred to in the content.